The filter and calibration wheel for the ATHENA wide field imager

M. Rataj, S. Polak, T. Palgan, T. Kamisiński, A. Pilch, et al.

M. Rataj, S. Polak, T. Palgan, T. Kamisiński, A. Pilch, J. Eder, N. Meidinger, M. Plattner, M. Barbera, G. Parodi, Fabio D'Anca, "The filter and calibration wheel for the ATHENA wide field imager," Proc. SPIE 9905, Space Telescopes and Instrumentation 2016: Ultraviolet to Gamma Ray, 990568 (11 July 2016); doi: 10.1117/12.2235411

Event: SPIE Astronomical Telescopes + Instrumentation, 2016, Edinburgh, United Kingdom

The Filter and Calibration Wheel for the ATHENA Wide Field Imager

M. Rataj[a], S. Polak[a], T. Palgan[a], T. Kamisiński[b], A. Pilch[b], J. Eder[c], N. Meidinger[c], M. Plattner[c], M. Barbera[d], G. Parodi[e], Fabio D'Anca[f]

[a]Space Research Center, Polish Academy of Sciences, Bartycka 18A, 00-716 Warsaw, Poland; [b]Department of Mechanics and Vibroacoustics, AGH University of Science and Technology, al. A. Mickiewicza 30, 30-059 Kraków, Poland; [c]Max-Planck-Institut fuer extraterrestrische Physik, Giessenbachstrasse, 85748 Garching, Germany; [d]Università degli Studi di Palermo, Dipartimento di Fisica e Chimica, Via Archirafi 36, 90123 Palermo, Italy; [e]BCV progetti s.r.l., via S. Orsola 1, 20123 Milano, Italy; [f]Istituto di BioFisica U.O.S. di Palermo, Consiglio Nazionale delle Ricerche, Via Ugo La Malfa 153, 90146 Palermo, Italy

ABSTRACT

The planned filter and calibration wheel for the Wide Field Imager (WFI) instrument on Athena is presented. With four selectable positions it provides the necessary functions, in particular an UV/VIS blocking filter for the WFI detectors and a calibration source. Challenges for the filter wheel design are the large volume and mass of the subsystem, the implementation of a robust mechanism and the protection of the ultra-thin filter with an area of 160 mm square. This paper describes performed trade-offs based on simulation results and describes the baseline design in detail. Reliable solutions are envisaged for the conceptual design of the filter and calibration wheel. Four different variant with different position of the filter are presented. Risk mitigation and the compliance to design requirements are demonstrated.

Keywords: Filter wheel mechanism, FEM structural and acoustic analysis, ATHENA, WFI

1. INTRODUCTION

One of the key instruments of ATHENA is the Wide Field Imager (WFI) which will provide imaging in the X-ray energy range of 0.2-15 keV over a field of view with the size of 40 arc min squared in combination with spectrally and time-resolved photon counting. The WFI detector, based on arrays of DEPFET active pixel sensors, is also sensitive to photons in the UV and VIS range. An appropriate blocking filter is thus needed for the large field of view detector as well as for the smaller high count rate capable detector of WFI.

The planned filter and calibration wheel will provide four positions, i.e. open aperture, optical blocking filter, closed position and calibration. The four positions can be individually aligned with the camera aperture. Since the camera has an extremely large detector with an aperture of 160x160 mm² and an additional small detector for fast measurements with an aperture of 15x15 mm², the aforementioned features have to be doubled.

Apart from the size the design of the filter wheel comprises other challenges. Due to the large geometry mass saving is a major issue, the housing and integrated front baffle shall however also serve as proton shield. Launch environment becomes critical with respect to high loads in case of dynamic coupling if the frequencies cannot be moved far enough away from the eigenfrequencies of the instrument structure. FEM analysis has been performed in order to optimize the structural design.

Another major issue is the protection of the large filter during AIT as well as during launch. Due to the complexity of the camera head with its high number of cables and heat pipes, a vacuum chamber as filter wheel housing shall be avoided. It is investigated whether the Filter Wheel can be in atmosphere during launch with localized protection of the filters, mainly with respect to acoustic load. Results of acoustic simulation analysis are presented in order to demonstrate that the filter will withstand environmental loads.

Space Telescopes and Instrumentation 2016: Ultraviolet to Gamma Ray, edited by Jan-Willem A. den Herder, Tadayuki Takahashi, Marshall Bautz, Proc. of SPIE Vol. 9905, 990568
 · doi: 10.1117/12.2235411

To reduce complexity and mass, simple but reliable solutions are envisaged including the mechanical configuration as well as the motor drive and position control. This paper will describe the various challenges and provide trade-offs that have been performed. The baseline concept that fulfils the design requirements is presented and selected solutions are describe in detail. The presented analysis are mainly focused on acoustic loads during launch phase.

2. FILTER WHEEL ASSEMBLY DESIGN VARIANTS

The Filter Wheel Assembly (FWA) is situated at the structure of the WFI as it shown on the Figure 1. The opposite side of FWA is visible on the next drawing (view from detector side) . The FWA contains the wheel with four positions, i.e. open aperture, optical blocking filter, closed position and calibration.

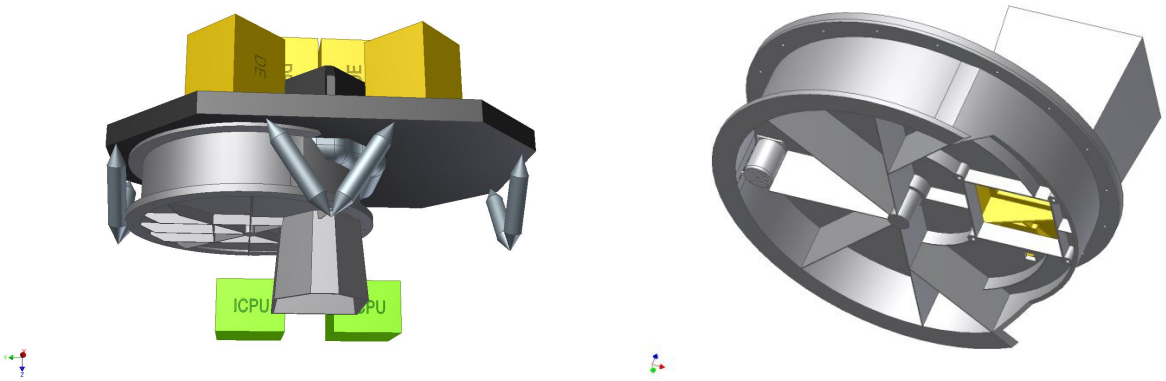

Figure 1 Left panel – position of the Filter Wheel Assembly at the structure. Right panel – view of FWA from the detector side

2.1 Spur gear wreath size

Basing on the design from previous phases of the Filter Wheel Assembly (FWA) of the WFI project, further design was made. One of issues was to calculate the spur gear, which transfer power from stepper motor into Filter Wheel (FW), providing its rotation. The most obvious design of spur gear was an internal spur gear located on the edge of FW. It's pitch diameter should be large enough to prevent covering the FOV of detector. This type of design provides gear ratio ~20:1, but it has drawbacks. To optimize design (lower inertia, lower mass), it was proposed to use smaller external spur gear located closer to centre of the filter wheel. With gear ratio ~10:1 it still provides acceptable accuracy of positioning, but mass of gear wreath itself was reduced . This has led to reduction of inertia, which means less power consumption of motor and more stiff structure (less tilting moments in bearings). Both solutions are shown in Figure 2

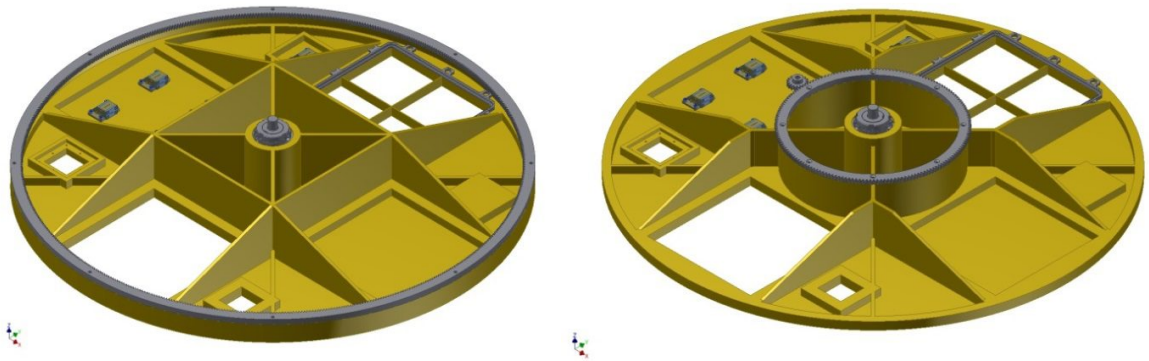

Figure 2 Left panel – first variant of FW with large gear wreath. Right panel– second variant of FW with small gear wreath.

2.2 Filter wheel position inside instrument chamber

Further design considerations led to minimize acoustic loads, which affect the filter. To prevent propagation of acoustic wave inside FWA it was proposed to place the filter wheel upside-down. During launch filter wheel will be in "closed" position, which may weak acoustic impact on filter. On Figure 3 four variants are presented – first two known from chapter 2.1; others are reversed previous ones.

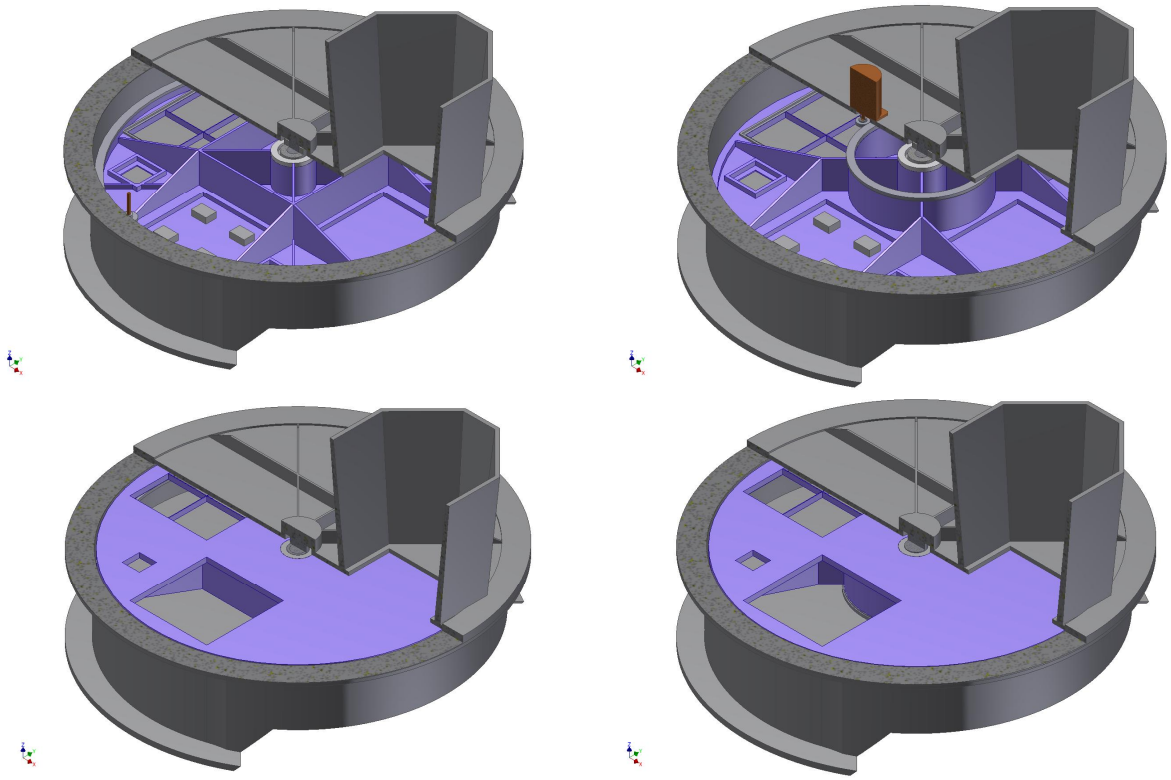

Figure 3 Design changes of FWA aimed to minimalize acoustic loads on filter. Upper left plane – first variant V1 (FW with large gear wreath). Upper right plane – second variant V2 (FW with small gear wreath). Lower left plane – third variant V3 (large gear wreath with reversed position). Lower right plane – fourth variant V4 (small gear wreath with reversed position).

2.3 Filter position on FW

In base design filter was located next to plugged area of FW. There was an assumption, that moving filter further from baffle may reduce the acoustic impact on the filter. To do this, new design with filter area replaced with calibration area was introduced.

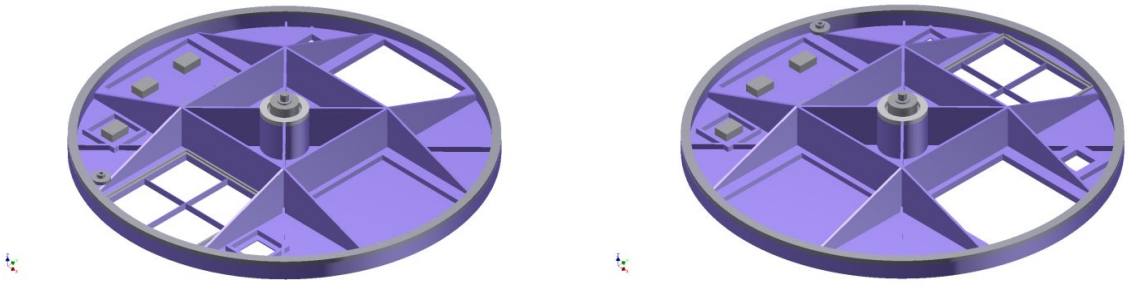

Figure 4 The location of filter area. Left plane – filter area next to plugged area. Right plane – filter area offset by 90° towards to base design.

For these variants simultaneously acoustic and FEM structural analysis were conducted.

3. ACOUSTIC ANALYSIS

The acoustic analysis were conducted for the acoustic loads for ARIANE 5 (see table below) specified by ESA.

Table 1. Acoustic loads.

Octave band centre frequency	Qualification level (dB)	Protoflight level (dB)	Acceptance level (dB)
(Hz)	Ref: 0 dB = 2 x10-5 Pascal		
31,5	131	131	128
63	134	134	131
125	139	139	136
250	136	136	133
500	132	132	129
1000	126	126	123
2000	119	119	116
Overall level	142.5	142.5	139.5
Test duration	2 minutes	1 minutes	1 minutes

The goal of analysis is to give guidance of design improvement to minimise acoustic loads into the filter. Proposed changes in design are calculated in FEM structural model to check resonance frequencies. All acoustic analysis were made taking into account acoustic-structure interaction between air and analysed FWA. In eigenfrequecy calculation, 20 first frequencies were found for both V2 and V4 variant filled with air. It was assumed, that top of the baffle is open, so the sound could be radiated from there. Detector side of the air filling FWA was set to be closed (sound hard boundary). From 40 frequencies, 36 unique values covering range 39-400 Hz were taken to the harmonic analysis, were plane wave sound source were defined in the end of approximately 30 cm high air cylinder above FWA connected to the whole surface of the top cover. Amplitudes of the plane wave were interpolated from loads for Ariane 5 (table 1).

Results of acoustic simulation analysis are presented in order to demonstrate that the filter will withstand environmental loads. The analysis was done for four variants (see Figure 3).

Results of acoustic simulation are presented on Figure 5. The average sound pressure level on surface where the filter would be mounted is the highest for 124 Hz, V1 and V2 – above 160 dB.

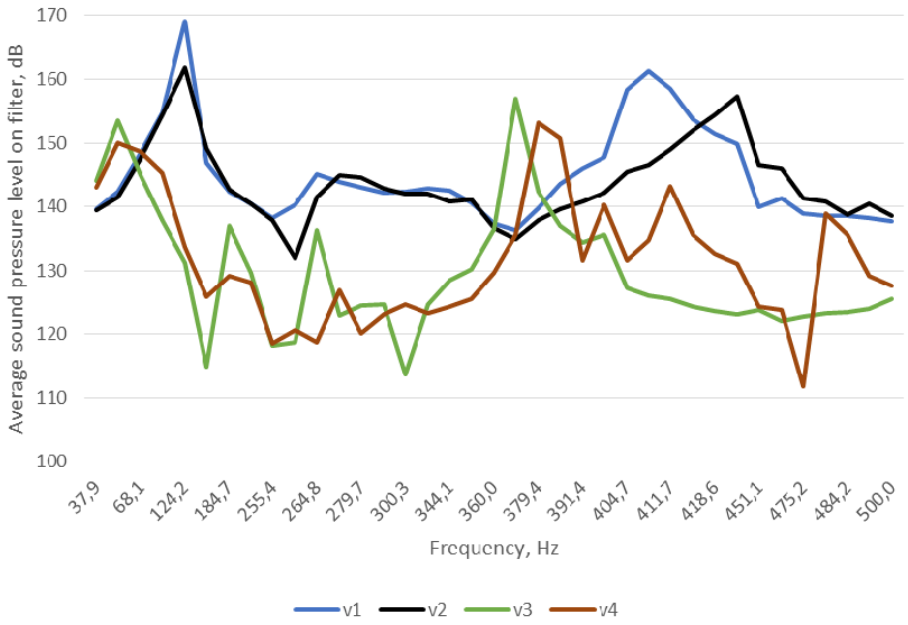

Figure 5 Average sound pressure level on filter for acoustic loads from Ariane 5.

From presented results it is visible that variants V3 and V4, it means the filter plane is in upper position, gives much lower values of sound pressure level in the place of filter. There are only two local peaks – for 49 Hz, and 379 Hz. The lower one (Figure 6) is connected with the eigenfrequency of the filter wheel – high amplitude vibrations are induced on it just under the baffle. Also for 379 Hz, there is some resonance frequency of the filter wheel (Figure 7). For variants V3 and V4, there is small difference in frequency of that resonance, what is caused by different position of the gear wreath.

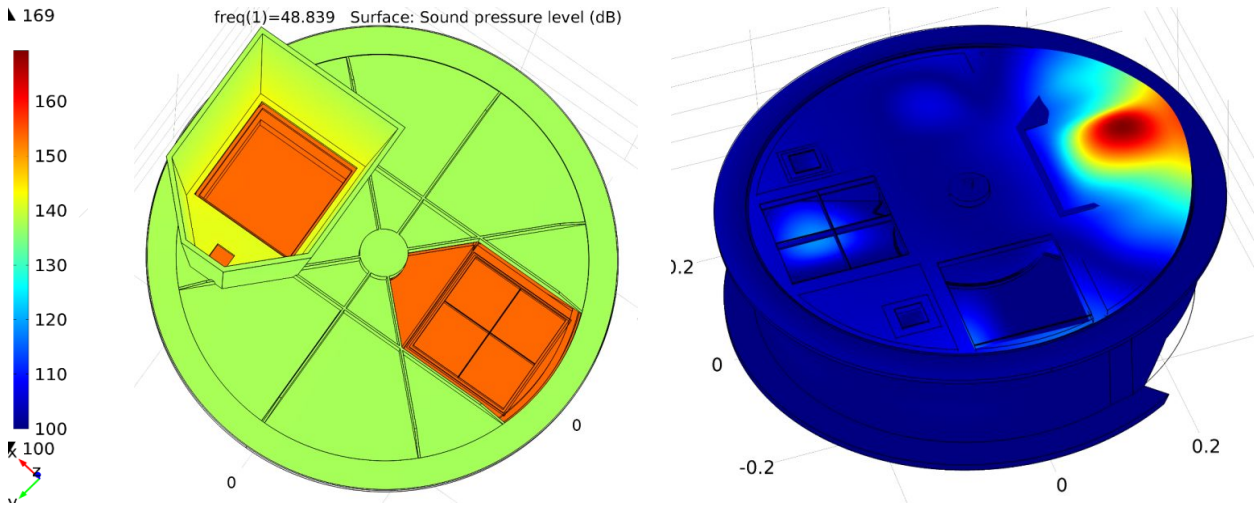

Figure 6 Left panel – sound pressure level distribution for 48Hz variant V4. Right panel – max displacement distribution of the filter wheel.

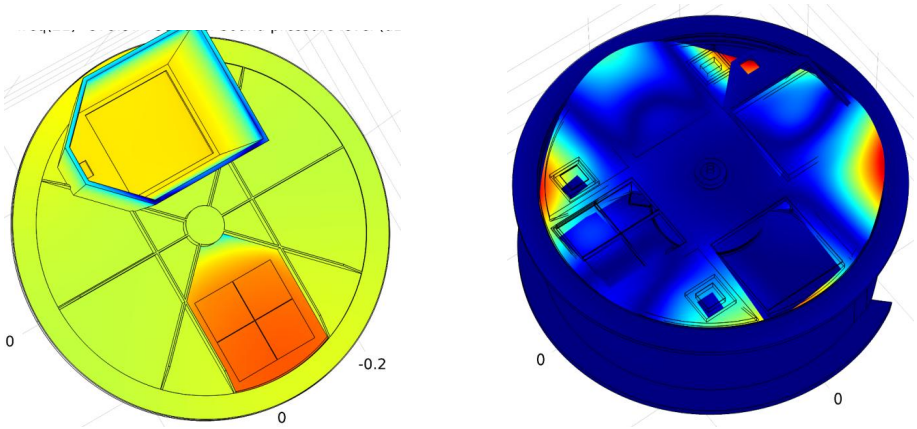

Figure 7 Left panel – sound pressure level distribution for 379Hz variant V4. Right panel – max displacement distribution

For further analysis these variants (V3 and V4) were selected. In next step increase of the thickness of wheel in front of baffle from 2 to 5 mm and sound absorbers were introduced and position of the filter (rotation about 90°)was changed.

Sound absorber was quite thin (only 17 mm). Rather light material was proposed (flow resistivity 30000 Pa*s/m). Delany–Bazley model was used to calculate characteristic impedance and wave number for that kind of material.

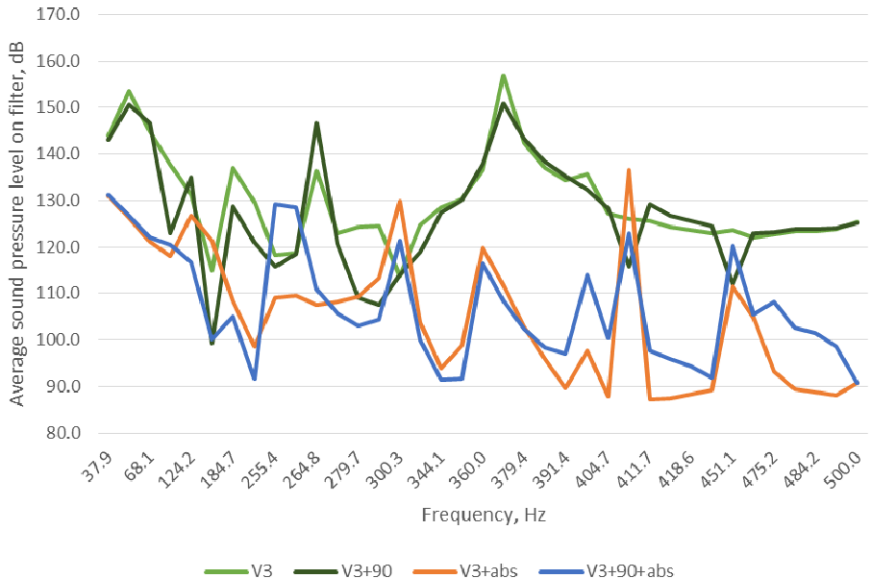

Figure 8 Influence of the filter wheel modification on the sound pressure level on filter. V3+90 – filter wheel moved by 90 degrees, V3+abs – filter wheel with sound absorber and thicker part under the baffle, V3+90+abs – filter wheel moved by 90 degrees with sound absorber.

Different position of the filter on the filter wheel gives similar results in sound pressure level (V3 and V3+90 in Figure 9). Modification of the filter wheel and adding sound absorber under the baffle gave a great improvement – acoustic energy is more than 20 dB lower at filter than before modification of the filter wheel. Resonance presented for V3, 379 Hz moved to 407 Hz, because of the increase of the stiffness of the filter wheel, where sharp peak is noticeable. Sound pressure level distribution for 407 Hz is presented in Figure 10 left panel. The total displacement of the FW for that frequency are very similar to presented in Figure 10 right panel for 379 Hz. There is also a resonance of the air in the cavity under filter wheel, what makes filter wheel vibrating. That is also a reason of high sound pressure levels on filter.

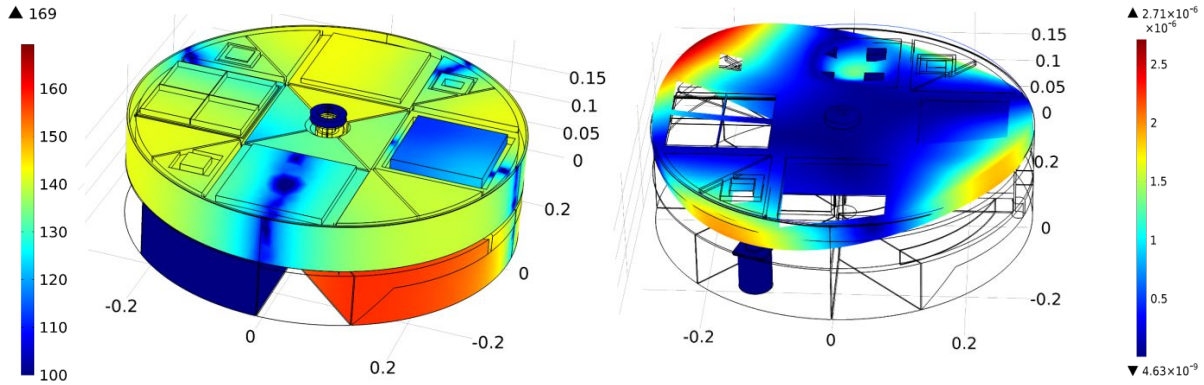

Figure 9 Left panel – sound pressure level distribution for V3+90+abs at 407 Hz. Right panel – total displacements of the filter wheel V3 with absorber at 397 Hz.

Different position of the filter on modified filter wheel, gives similar sound pressure level on the filter (V3+90+abs). Sharp peak at 407 Hz is lower, but there are higher values for another frequencies (about 250 Hz, above 480 Hz).

4. FEM STRUCTURAL ANALYSIS OF THE FILTER WHEEL

A detailed design of the FW structure is required in order to identify the structural behaviour of the unit. Following this philosophy, the unit subassemblies were simplified and merged to make one part. The threaded connections were removed and little holes were fulfilled with base material. Very little steps were removed also.

The three cases are considered (see figure 10):

1. FW with small gear wreath; the filter located on opposite side of the baffle;
2. FW with large gear wreath, the filter located on opposite side of the baffle;
3. FW with large gear wreath, the filter located at the position angle 90 deg from the baffle;

The complete FEM is made using ANSYS Workbench v11 software. Number of nodes: 253350; number of elements: 72486. The FWA is mounted on panel so it was assumed that its connection is rigidly fixed. For vibration analysis level of 20g static load was assumed.

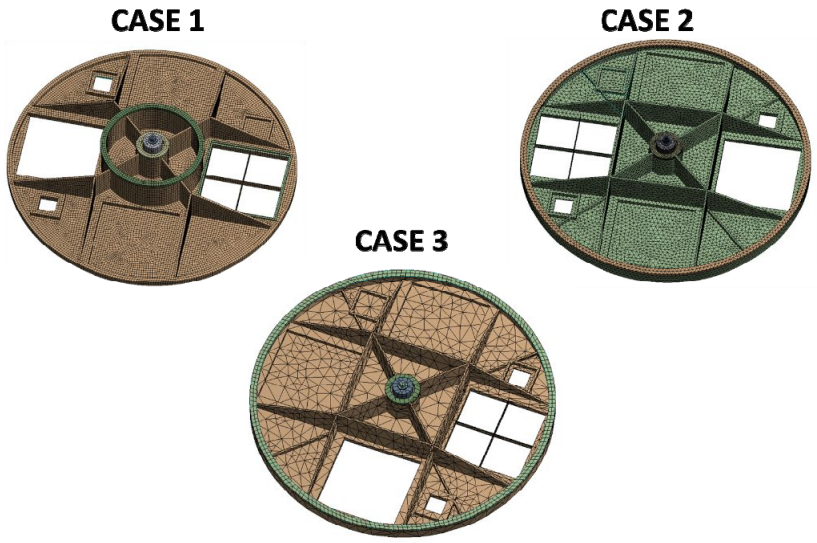

Figure 10 Considered cases of FEM structural analysis.

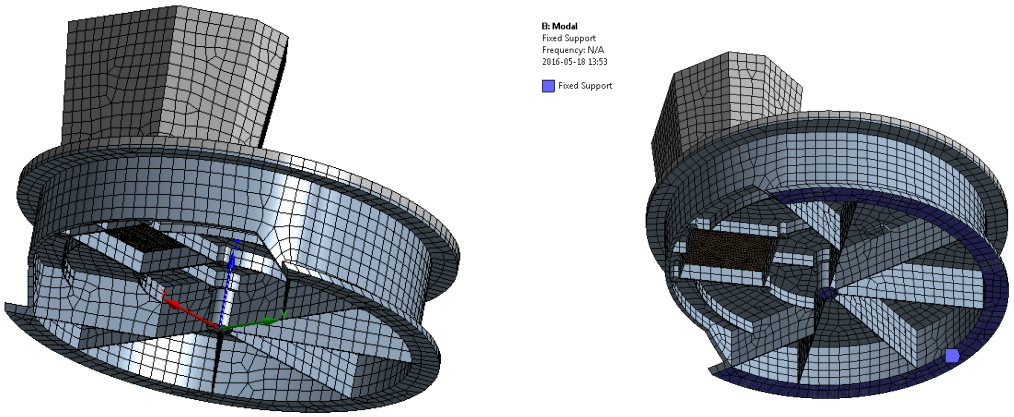

Figure 11 Left panel – coordinate system. Right panel – fixed support (blue surface).

4.1 Results of modal Analysis

The presented tables shows analysis for the first six modes. The goal for this analysis was to define modes and its impact for the structure. At tables are presented only these frequencies which have an impact on the FW. The effective mass vs. total mass-ratio are checked to determine how is the impact of the masses during mode. Effective mass-ratio provide the information which frequencies are critical for the construction for firs six modes.

Table 2. Effective mass / total mass in Case 1.

Mode	Frequency [Hz]	Effective mass / total mass						Order of importance
		X-direction	Y-direction	Z-direction	rotation X	rotation Y	rotation Z	
1	203,97	0,000	0,000	0,000	0,000	0,000	0,099	5
2	254,75	0,001	0,000	0,001	0,002	0,008	0,000	6
3	287,22	0,018	0,000	0,001	0,002	0,124	0,000	3
4	314,51	0,000	0,019	0,000	0,090	0,000	0,003	4
5	355,36	0,084	0,009	0,021	0,021	0,229	0,007	1
6	368,08	0,026	0,020	0,000	0,056	0,066	0,005	2

The biggest effective masses for the Case 1 is identify in mode 5 frequencies for this equal 355,36 Hz. This is generated by the filter wheel, and the rotation in Y axis [Table 2.] provide the modal shape for this mode.

Table 3. Effective mass / total mass in Case 2.

Mode	Frequency [Hz]	Effective mass / total mass						Order of importance
		X-direction	Y-direction	Z-direction	rotation X	rotation Y	rotation Z	
1	165,83	0,000	0,000	0,000	0,000	0,000	0,139	4
2	279,71	0,027	0,001	0,004	0,004	0,225	0,000	3
3	291,71	0,000	0,022	0,000	0,147	0,003	0,003	5
4	361,18	0,000	0,000	0,000	0,000	0,000	0,000	6
5	369,43	0,093	0,024	0,014	0,051	0,176	0,021	1
6	387,40	0,110	0,020	0,002	0,045	0,180	0,009	2

The biggest effective masses for the Case 2 is identify in mode 5 frequencies for this equal 369,43 Hz. This is generated by the filter wheel, and the rotation in Y axis [Table 3.] provide the modal shape for this mode. However the other directions have the significant impact on the mode shape.

Table 4. Effective mass / total mass in Case 3.

Mode	Frequency [Hz]	Effective mass / total mass						Order of importance
		X-direction	Y-direction	Z-direction	rotation X	rotation Y	rotation Z	
1	196,97	0,000	0,000	0,000	0,000	0,000	0,174	3
2	319,76	0,087	0,005	0,016	0,017	0,432	0,002	1
3	335,46	0,003	0,066	0,000	0,258	0,015	0,012	2
4	396,24	0,080	0,008	0,014	0,009	0,112	0,012	4
5	411,33	0,060	0,014	0,002	0,021	0,084	0,009	5
6	501,90	0,010	0,008	0,025	0,010	0,003	0,005	6

The biggest effective masses for the Case 3 is identify in mode 2, frequencies for this equal 319,76 Hz. This is generated by the filter wheel, and the rotation in Y axis [Table 4.] provide the modal shape for this mode.

Important modes plots shapes for the selected frequencies are presented in Figures 12 - 14.

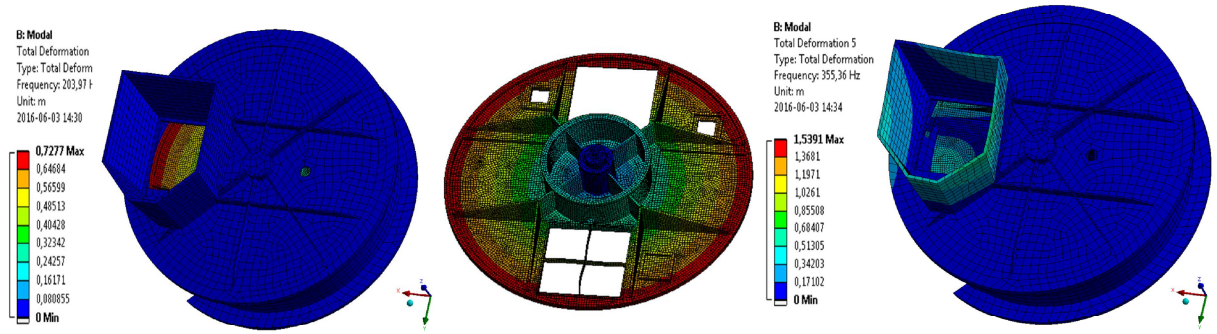

Figure 12 Left and center panel – Case 1 Mode 1 with and –without cover. Right panel – Case 1 Mode 5

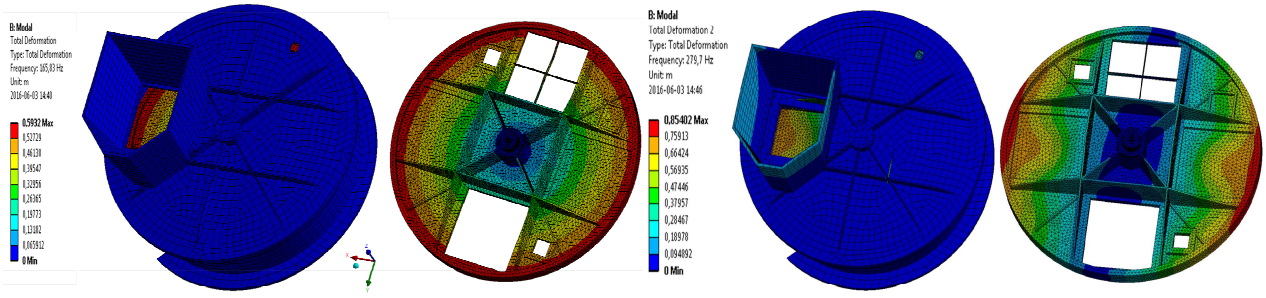

Figure 13 Left and center panel – Case 2 Mode 1 with and –without cover. Right panel – Case 2 Mode 2 same as before.

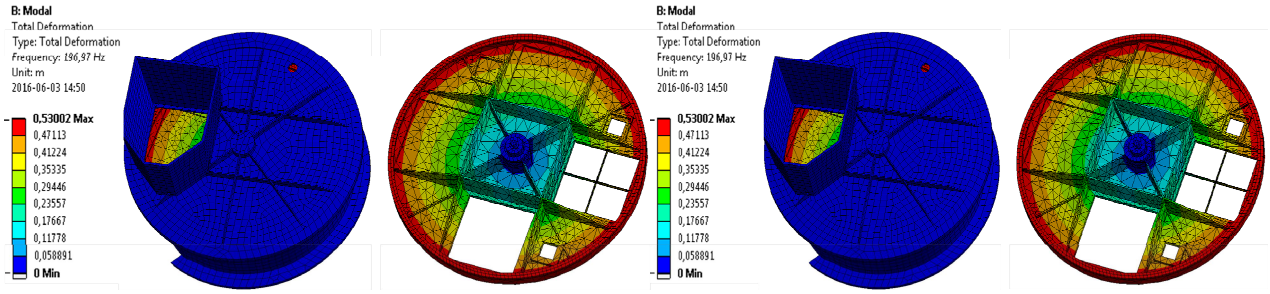

Figure 14 Left and center panel – Case 3 Mode 1 with and –without cover. Right panel – Case 3 Mode 2 same as before.

4.2 Sine 20G Analysis

Harmonic response analysis was made in frequency range 5-100 Hz with acceleration amplitude 20g along x, y and z axis. The goal for this analysis is to define the stress behaviour for the structure under dynamic load.

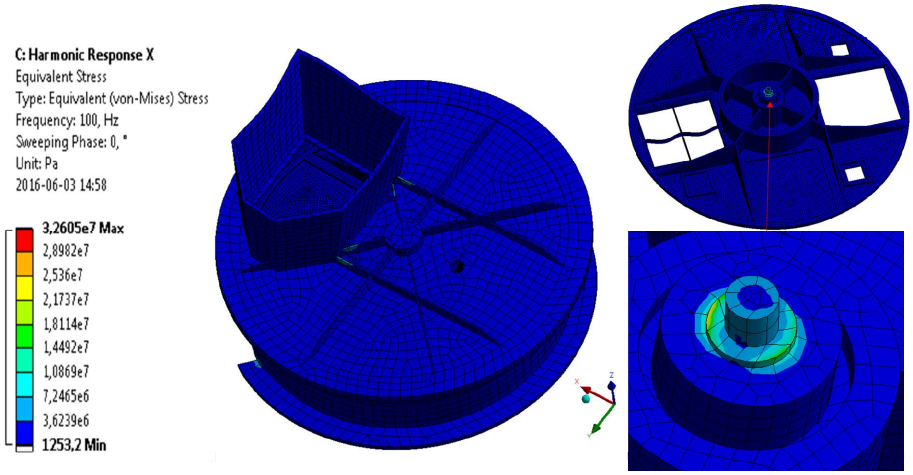

Figure 15 Sine 20G X – Axis results.

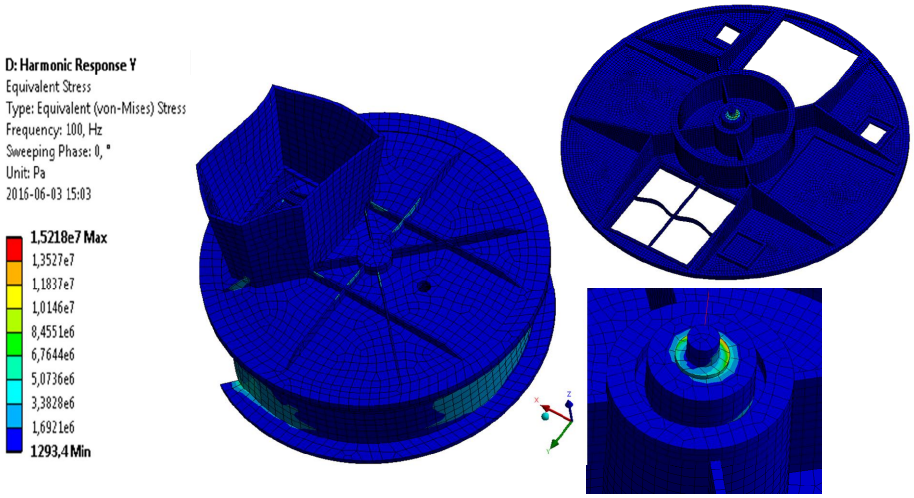

Figure 16 Sine 20G Y – Axis results

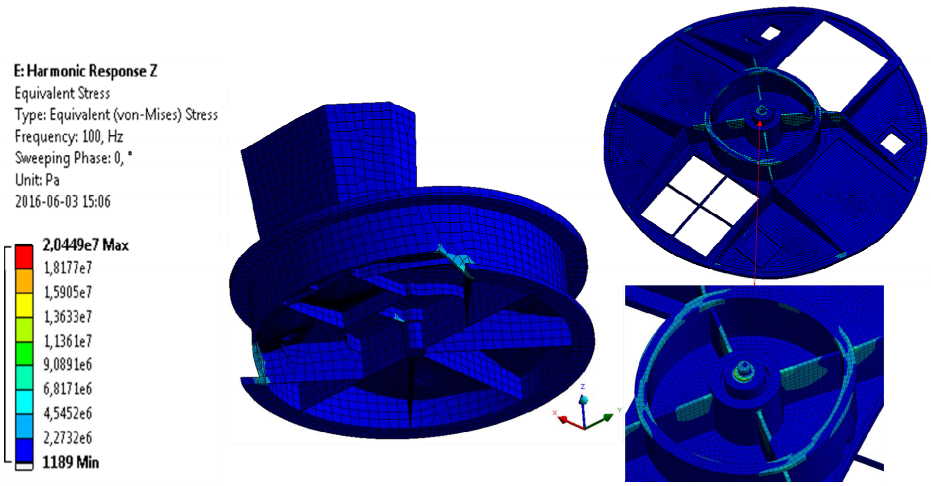

Figure 17 Sine 20G Z – Axis results.

The summary of modal and sine 20 g is presented in Table 5.

Table 5. Filter wheel FEM analysis summary.

FW Analysis Summary				
Frequencies [Hz]	Mode	Case 1	Case 2	Case 3
	1	204,0	165,8	197,00
	2	254,8	279,7	319,8
	3	287,2	291,7	335,5
	4	314,5	361,2	396,2
	5	355,4	369,4	411,3
	6	368,1	387,4	501,9
SINE [MPa]	X-Axis	28,9	30,1	7,5
	Y-Axis	13,5	11,7	8,8
	Z-Axis	18,2	23,7	6,8

4.3 Conclusion

The analysis shown above identify the modal behavior for the filter wheel assembly. Based on modal analysis the case 3 have the best modal results. The first modes was calculated for the separately cases. Based on received results we see that, the filter wheel generate modes at first. The effective masses for this modes are not too high. The dangerous frequencies for the structure are above 500 Hz. The sine analysis shows that the construction is very stiff, the maximum von Misses stress is identified in the bearings.

5. THE FILTER AND MESH ANALYSIS

The filter is composed by a thin polyimide film and by a reinforcing metallic mesh glued together. They are the structural components sustaining the real filter, consisting of a thin Al layer, which does not help in supporting the mechanical loads.

A cross shaped central stiffening, matching the gaps between the four WFI detector quadrants, divides the filter in four equal areas as shown in figure 5.4. Two different configurations are presently studied. The first one (left panel) consists of the inner supporting frame (1), the outer supporting frame (2), the SS mesh (3), the aluminium coated polyimide film (4). In the second configuration (right panel) the mesh with larger pitch and larger and thicker wires is made of aluminum and is integrated in the inner supporting frame (1), the outer frame (2) and the polyimide film (3) are as in the other configuration.

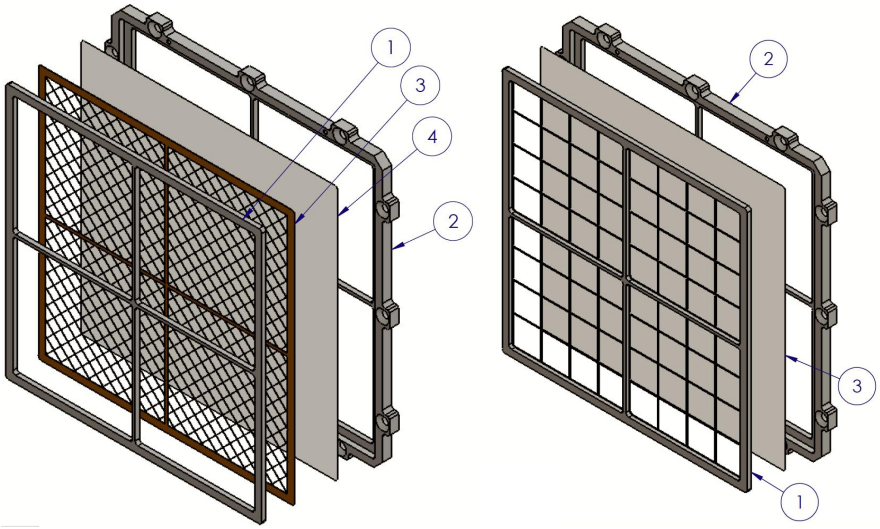

Figure 18 WFI filter configuration used in numerical analyses (left) and alternative option having larger mesh cells realized in Al alloy (right)

Figure 1 shows the configuration 1 with all its components integrated together. As it evident the mesh wires are parallel to the filter diagonals. This design, as previously shown (Barbera et al 2014 see reference below), reduces significantly the maximum stress on the wires.

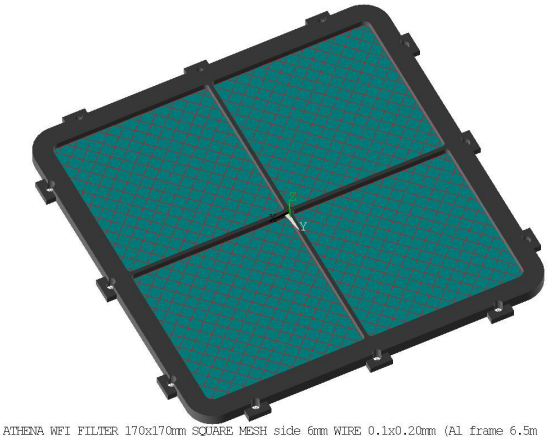

Figure 19 WFI filter configuration used in the numerical analyses. The mesh is stainless steel and is glued to the polyimide film on one side and to the inner frame on the other side.

All preliminary numerical results, reported hereafter, refer to one of the different candidate configurations currently under examination, having the geometry described in the following table. In the analyses the filter wheel has been considered as infinitely stiff.

Table 6. Main characteristics of the filter configuration simulated with numerical analysis.

Full filter size	170×170 mm	Mesh material	Stainless steel
Frame material	Al alloy 10×6.5 mm cross section (width×thick.)	Mesh cell	Square shaped, 6.1mm side, parallel to frame diagonals
Central stiffenning	2×6.5 mm cross section (width×thick.)	Mesh wire cross section	100×200μm (w×t)
Structural film	Polyimide 150 nm thick	Connection to FW	12 screws
Filter	Al deposit (not structural)		

The structural design of the filter film and of the mesh, under mechanical and acoustic loads, represents a very challenging task due to many existing criticalities, as for instance the extreme fragility of the film, the large filter size, the complexity of its structural behaviour under dynamic random loads, the grey areas, existing uncertainties and lack of knowledge.

Main criticalities and possible mitigation actions are briefly commented hereafter. In any case it is clear that, in so complex problems, the experimental proofs represent the main tool to develop and validate the design.

We plan to perform in the near future acoustic tests and vibration tests of sample filters mounted on a mechanical structure similar to the Filter Wheel. The first tests will be performed on filters having the proper configuration depicted in Figure 18 but using a thicker film (~ 1 μm) of stretched polypropylene in place of the thin (150 nm) Polyimide films. Such preliminary tests will serve as a guide to tune the mechanical design of the FW and filter without running the risk to damage very expensive filters.

We have set-up the facility to stretch in house the polypropylene, we have started the construction of the filter frames (see Figure 20), and plan to procure in the near future the SS meshes and start soon the integration of the filters. Acoustic and vibration tests are planned in Q3-Q4 2016.

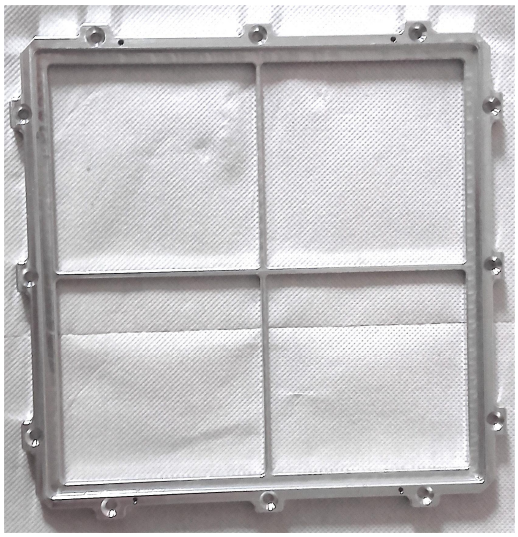

Figure 20 Outer frame of the WFI filter manufactured in Al alloy with a high speed milling machine.

5.1 Knowledge of the constitutive model of the materials

Polymeric materials, like polyimide, do not show the basic Hookean behavior but they are visco-elastic materials. The stiffness modulus of these kind of materials is not constant; it varies with the strain amplitude, the strain rate and it shows creep phenomena. Also the instantaneous thickness does not remain fixed but it changes with the stretching of the film.

In principle such behaviour would make the stress analysis very complex. Moreover the constitutive law of the film is unknown. The candidate Manufacturer makes available just the following data at room temperature:

- Density 1.41-1.47 g/cm^3
- CTE 3×10^{-6} K^{-1}
- Tensile strength 310 MPa
- Tensile elongation 22%

On the other hand, the lack of long time loads which could induce creep phenomena and the cyclic dynamic loads, suggests the need to maintain low stress level, below the elastic limit. Lacking precise data for our material, the elastic limit has been roughly assumed at 70 MPa for similarity to such kind of materials. For this reasons the film has been considered as linear elastic in the analyses.

Also the reinforcing mesh stress level has to be maintained in the elastic range. So also the mesh has been considered elastic too.

No data are available about the strength under cyclic loads (fatigue) which are typical of our application. An experimental proof campaign is needed to derive the reducing factor to be applied for taking into account fatigue phenomena.

5.2 Impact of defects on stress peaks in the film

No data are available about the presence of local defects which give rise to local stress peaks in the film. At the moment we see two main sources of stress concentrations:

- Local defects in the film itself;
- Local defects in the connection between the film and the reinforcing mesh, (irregularities of the adhesive geometry or local lack of adhesive).

Just to test the sensitivity of the elastic stress peaks to defects in the adhesive connecting the film to the reinforcing mesh, we defined four reference defects respect to the nominal adhesive shape, consisting in a continuous fillet 0.1mm wide.

The geometry of the four reference defects, quoted in mm, are detailed in the picture below. They have been applied to an elementary cell of a square reinforcing mesh 6×6 mm size, connected by adhesive along the whole wire width (0.1mm). The film is 150nm thick.

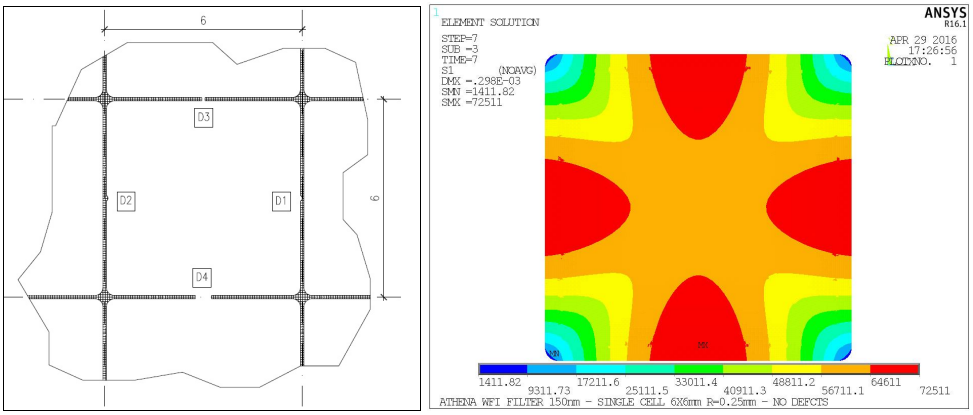

Figure 21 Pattern on the defects (left). Principal tensile stress in the nominal configuration, without any defects in the adhesive, quoted in kPa (right) under 10 mbar pressure. Maximum tensile principal stress is 72.5 MPa at side midpoints. Such value represents the reference to assess the severity of the adhesive defects.

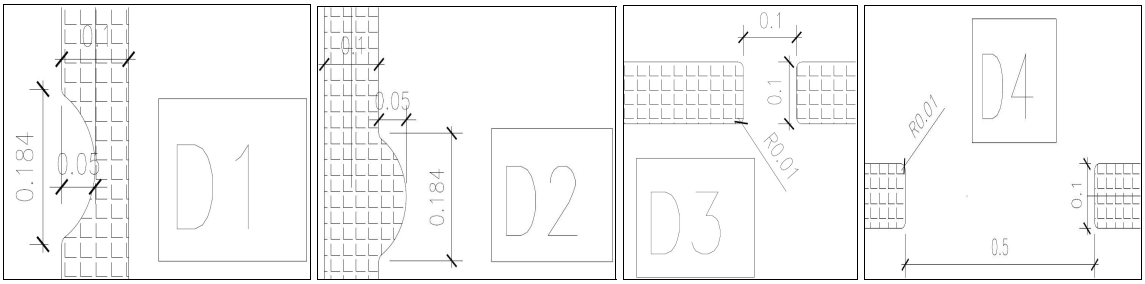

Figure 22 Defects D1 and D2 consist in a local adhesive lack or bulging whose size is one half of the fillet width, defects D3 and D4 consist in a disruption of the adhesive fillet respectively 0.1 or 0.5mm long.

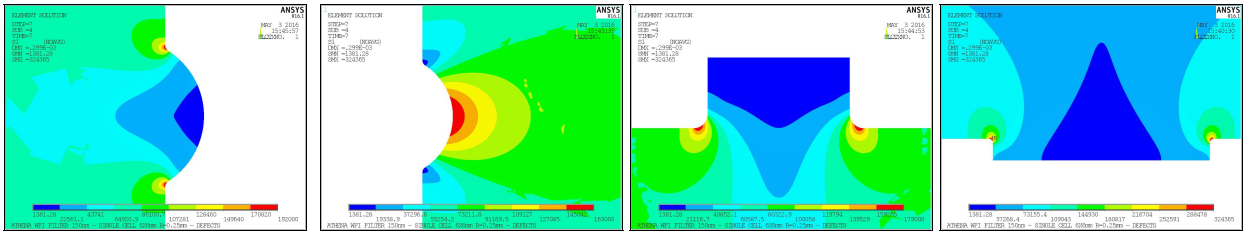

Figure 23 Principal tensile stress contours around the defects D1 to D4 (left to right) quoted in kPa. Elastic stress peaks values are 192 / 163/ 179 / 324 MPa respectively for defects from D1 to D4.

Results in the picture show that the elastic stress concentration factors for defects from D1 to D4 are respectively equal to 2.65 / 2.25 / 2.47 / 4.47. Finally, the results reported above point out that in case of non homogeneity of the adhesive connections, pressure loads (acoustic loads) give rise to severe stress concentration effects.

Obviously, as the elastic limit of the material is exceeded, the inelastic strains mitigate such stress peaks, but repeated overruns in the inelastic range under cycling loads could trigger the film failure.

More information about expected defects (position, shape and size) will be necessary to apply some reducing factor to the elastic limit, for taking into account defects in the film. Also in this case no data concerning potential stress raisers in the film are currently available, that make essential a proper experimental test campaign to validate any proposed design.

5.3 Structural behaviour

Filter and reinforcing mesh design are characterized by the extremely small thickness. In such conditions the “structure” doesn’t sustain distributed loads (pressure or inertia loads generated by acceleration normal to the filter plane) by bending as in a plane plate, but by membrane stresses.

Under a load “p” the filter deforms making the sag “s”. Internal stresses “q” hang the load to the outer frame constraints (Figure 24).

The stiffness of the system (and so the frequencies) depends on the sag and so on the applied load. Sag “s” characterizes the stiffness of the system: as the sag increases the stiffness increases too and smaller hanging stress Δq are necessary to sustain the same Δp.

In these conditions it is necessary to take into account the deformed shape in stress analyses. The analyses became non-linear for geometry.

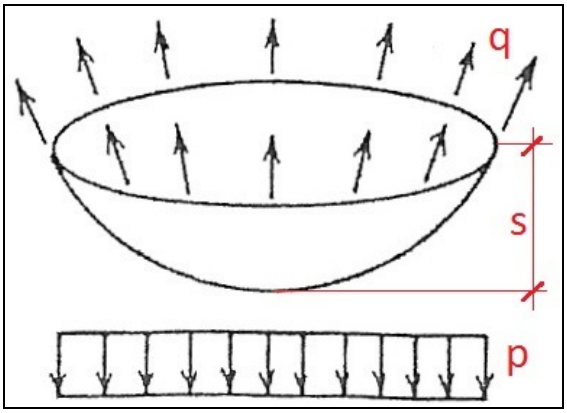

Figure 24 Membrane concept.

The non-linearity of the system is pointed out in the pictures below.

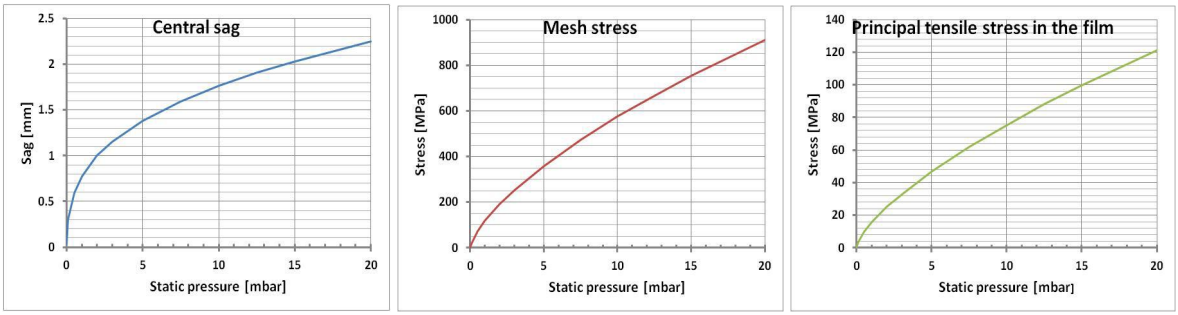

Figure 25 From left to right: central sag, maximum normal stress in the reinforcing mesh and maximum principal tensile stress in the film as function of the applied static pressure.

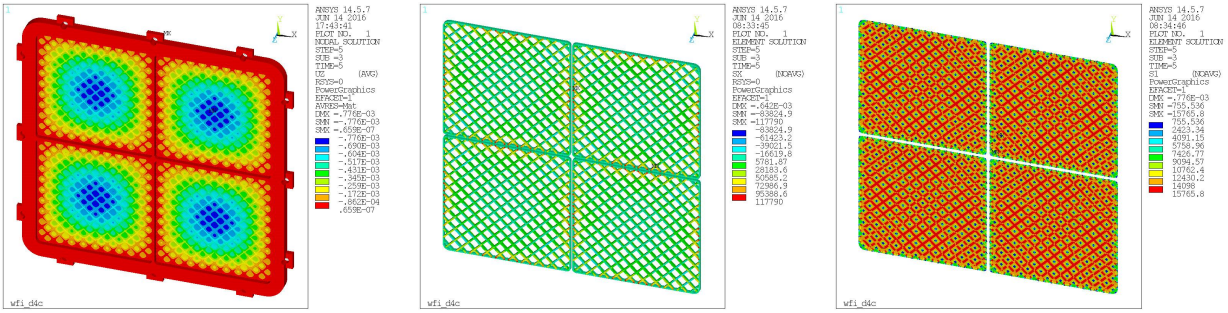

Figure 26 From left to right: contours of: deflection [m], the normal stress in the reinforcing mesh [kPa] and principal tensile stress in the film [kPa] under 1 mbar static pressure.

Contours of normal stresses in the mesh point out that maximum stresses occur at the connection to the frame, due to the bending moments generated by fixed conditions.

Being the structural behaviour non linear frequency values strongly depend on the applied load as shown in the picture below. Such non linearity affects the answer to dynamic loads. So the classical approach (psd analyses based on modal combinations) used to analyse the answer to acoustic loads and random vibrations, cannot be used simply as it is, since they are based on a linear structural behaviour.

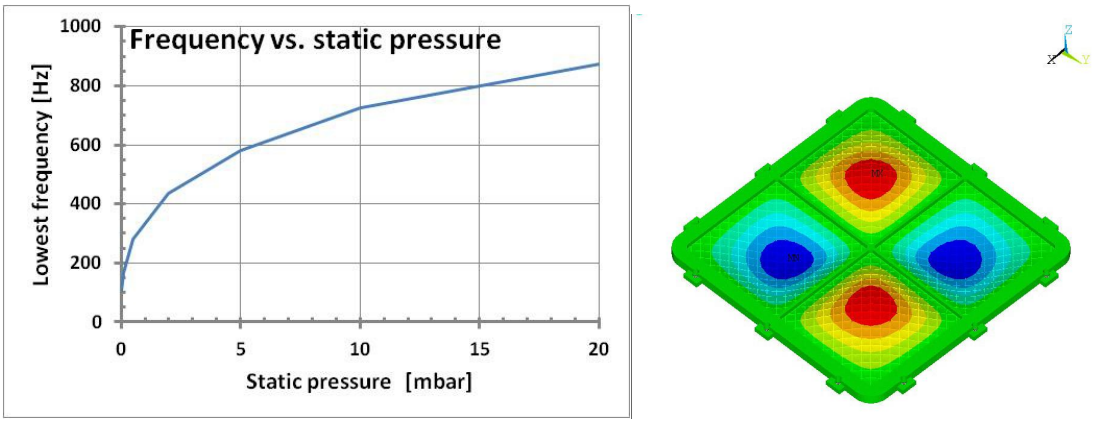

Figure 27 First frequency of the filter as function of the applied static pressure (left) and relevant modal shape (right). Contours refer to out of plane displacements.

To avoid too complex analyses, given that materials should be kept elastic, we have adopted a coarse simplified approach, which consists in carrying on the usual linear psd spectrum analyses for different levels of static pressure "p" (i.e. for different filter configuration in terms of sag "s" and internal membrane stresses "q"). When the maximum deflection (sag "s") computed by psd analysis for a stated pressure level, comes equal to the maximum displacement computed for the same static pressure, that identifies the configuration assumed as representative of the real behaviour at 1σ. Stress in film and mesh (1σ) are computed for that pressure level.

Picture below summarizes such approach, which has been carried out for the ARIANE 5 acoustic pressure at qualification level.

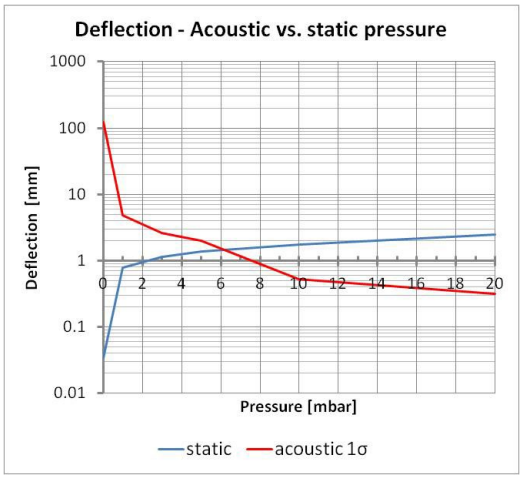

Figure 28. According to the simplified and coarse approach described, stress levels (1σ) should be derived from a psd analysis based on frequencies and modal shapes computed for a static pressure equal to about 6 mbar.

The final analyses will be carried out on the real expected dynamic load levels, when available.

5.4 The filter frame dynamic analysis

The goal for the analysis is to determinate the filter frame behavior during dynamic analysis. For analysis was taken second configuration of the supporting frame. The harmonic response (Sine 20 g) analysis selected to determinate the filter frame behavior.

The two options are checking to determine the stiffness of the construction:

- FW with large gear wreath, the filter located on opposite side of the baffle;
- FW with large gear wreath, the filter located at the position angle 90 deg from the baffle;

Boundary conditions

The fixed support (6 DOF are blocking) boundary conditions applied to the bottom cover surface. The loading 20 g (196,14 m/s^2) applied to the X,Y,Z axis of the FE model. The boundary conditions present on the Figure.18 for the Z axis like example.

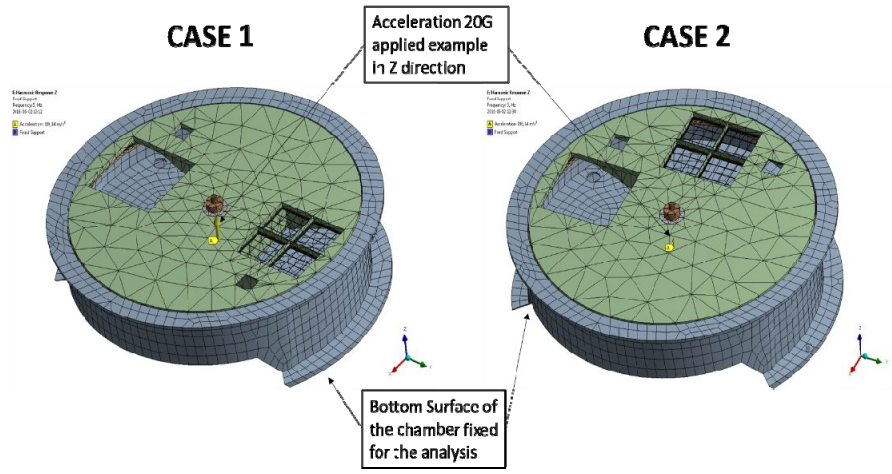

Figure 29 Boundary conditions for two cases of the filter frame (without top cover).

5.5 Results of the filter frame analysis.

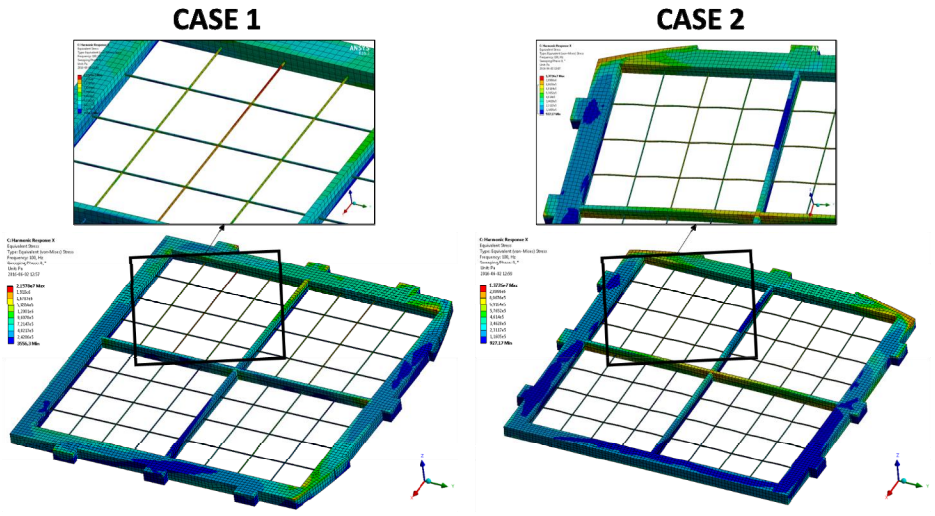

Figure 30 Von Missess Stress for X- direction for two cases of the filter frame location.

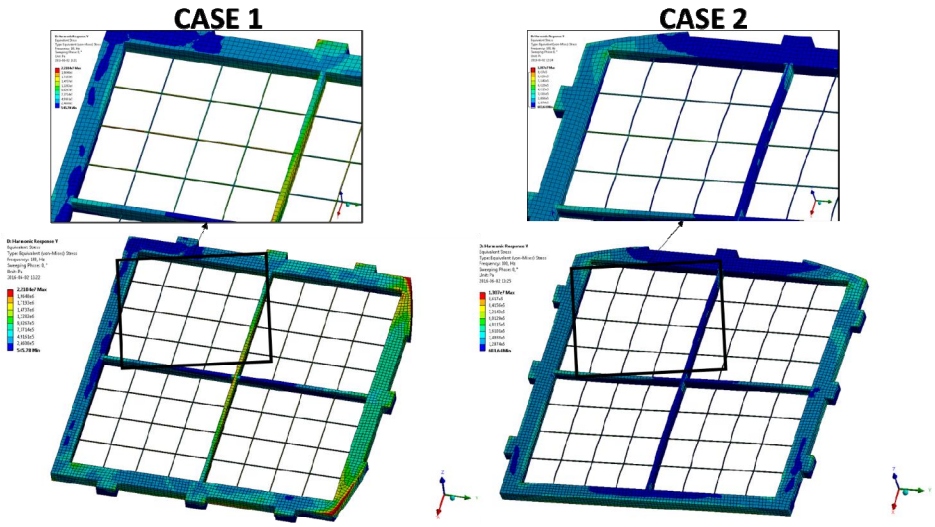

Figure 31 Von Missess Stress for Y- direction for two cases of the filter frame location.

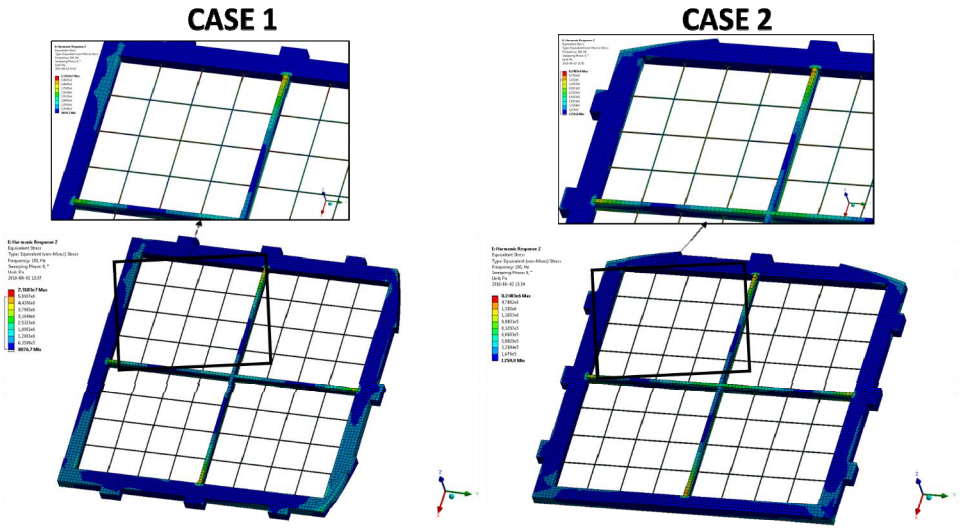

Figure 32 Von Missess Stress for Y- direction for two cases of the filter frame location.

Table 6. Von Misses stress results comparison for two cases.

Load	Von Misses Stress results [MPa]	
Sine 20 g	Case 1	Case 2
X – direction	21,5	13,7
Y – direction	22,1	13,0
Z – direction	23,1	8,2

The two considered cases are acceptable based on stress requirements for the material used for the structure. The filter frame is made from aluminium; the yield strength is Re=503 MPa, the filter film made for example polyimide have yield strength Re=70 MPa in 23°C. The received von Misses stress results present in table 6.

6. CONCLUSIONS

Presented results of analysis are first stage of the design of the Filter Wheel Assembly. Results show direction of further detail analysis. The analysis went into two directions. First one – minimalize of acoustic loads by the special design of the structure and the filter wheel and second one – improvement of resistance of the filter on the acoustic loads. For first direction best position of the filter was selected and solutions which reduce acoustic loads. Second direction of analysis described in the paper was focused on the acoustic analysis of the filter and comparison two mesh solutions. Preliminary conclusion from presented analysis is - the vacuum chamber as the filter wheel housing can be avoided. More detail analysis with further design optimization (lower inertia, lower mass) will be continued in next phase of the project.

7. ACKNOWLEDGEMENTS

Polish part of the research was realized within a framework of the project UMO-2015/18/M/St9/00541 “Polish Contribution In Scientific Development New X-Ray Telescope ATHENA” sponsored by Polish National Scientific Council.

The Italian research leading to these results has received funding from ASI (Italian Space Agency) through the Contract n. 2015-046-R.0 and from the European Union’s Horizon 2020 Programme under the AHEAD project (grant agreement n. 654215).

REFERENCES

[1] M. Barbera ; G. Branduardi-Raymont ; A. Collura ; A. Comastri ; J. Eder ; T. Kamisiński ; U. Lo Cicero ; N. Meidinger ; T. Mineo ; S. Molendi ; G. Parodi ; A. Pilch ; L. Piro ; M. Rataj ; G. Rauw ; L. Sciortino ; S. Sciortino ; P. Wawer; The optical blocking filter for the ATHENA wide field imager: ongoing activities towards the conceptual design. Proc. SPIE 9601, UV, X-Ray, and Gamma-Ray Space Instrumentation for Astronomy XIX, 960109 (August 24, 2015); doi:10.1117/12.2189326